Advances in Applied Mathematics and Mechanics
Adv. Appl. Math. Mech., Vol. **8**, No. 4, pp. 670-692

DOI: 10.4208/aamm.2014.m469
August 2016

Osher Flux with Entropy Fix for Two-Dimensional Euler Equations

Huajun Zhu[1,*], Xiaogang Deng[2], Meiliang Mao[1,3], Huayong Liu[1] and Guohua Tu[1]

[1] *State Key Laboratory of Aerodynamics, China Aerodynamics Research and Development Center, Mianyang, Sichuan 621000, China*
[2] *National University of Defense Technology, Changsha, Hunan 410073, China*
[3] *Computational Aerodynamics Institute, China Aerodynamics Research and Development Center, Mianyang, Sichuan 621000, China*

Received 21 January 2014; Accepted (in revised version) 3 July 2015

Abstract. We compare in this paper the properties of Osher flux with O-variant and P-variant (Osher-O flux and Osher-P flux) in finite volume methods for the two-dimensional Euler equations and propose an entropy fix technique to improve their robustness. We consider both first-order and second-order reconstructions. For inviscid hypersonic flow past a circular cylinder, we observe different problems for different schemes: A first-order Osher-O scheme on quadrangular grids yields a carbuncle shock, while a first-order Osher-P scheme results in a dislocation shock for high Mach number cases. In addition, a second-order Osher scheme can also yield a carbuncle shock or be unstable. To improve the robustness of these schemes we propose an entropy fix technique, and then present numerical results to show the effectiveness of the proposed method. In addition, the influence of grid aspects ratio, relative shock position to the grid and Mach number on shock stability are tested. Viscous heating problem and double Mach reflection problem are simulated to test the influence of the entropy fix on contact resolution and boundary layer resolution.

AMS subject classifications: 65M06, 65M70

Key words: Osher flux, entropy fix, Euler equation, finite volume method, "carbuncle" shock.

1 Introduction

Upwind schemes based on the characteristic theory have been widely used in solving the Euler equations for their capability of capturing discontinuities. Upwind schemes are usually classified into flux-vector and flux-difference splitting schemes. Flux-difference

*Corresponding author.
Email: hjzhu@skla.cardc.cn (H. J. Zhu)

 ©2016 Global Science Press

https://doi.org/10.4208/aamm.2014.m469 Published online by Cambridge University Press

splitting schemes such as Osher scheme [1,2] and Roe scheme [3] have gained popularity as they are robust and can capture steady discontinuities. Since the Osher scheme can capture steady discrete shock sharply [4–7], it has been widely used in fluid dynamics simulations [8–11]. There have been many numerical evidences showing the superiority of the Osher flux. For instance, Qiu et al. has done lots of work in [12–14] to compare the Osher fluxes with others recently, including Lax-Friedrich (LF), Godunov, Harten-Lax-van Leer (HLL), HLLC which is a modification of the HLL. They found that among these considered fluxes the Osher flux is the most robust one and has the best resolution near discontinuities. In addition, the Osher flux is also compared with the LF flux and the Vijayasundaram flux by Felcman and Havle in [15], which also shows that the numerical results obtained by the Osher scheme is the most accurate one.

For a supersonic blunt body problem, it was shown that the Roe's splitting produces a "carbuncle" schock (see [16, 17]). To solve this problem many efforts have been made. For instance, Lin proposed a cure by adding dissipation in linear waves to Roe's Riemann solver [18]. Sanders developed H-corrections based on the difference of the characteristic speeds on five interfaces [19]. Pandolfi and Ambrosio added appropriate dissipation according to the maximum difference between the characteristic speeds across the four interfaces [20]. Ren proposed a rotated Roe scheme based on the rotated Roe's approximate Riemann solver [21]. For Euler equations, the Osher flux takes a path integral of flux derivative in phase space. The integral subpaths are constructed based on the eigenvalues in decreasing order by Osher [4] and in increasing order by Spekreijse [22], which are referred to as the Osher-O flux and the Osher-P flux, respectively. There are already some investigations about the properties of these two different fluxes. For instance, Jacobs found that it is difficult to apply the Osher scheme for strong shock computations and proposed a 3-stage approximate Riemann solver at the cost of computations [23]. Amaladas and Kamath compared six kinds of upwind schemes based on steger-Warming, van Leer, Roe, Osher-P, AUSM and HUS, respectively [24]. It is indicated that the Osher schemes with O-variant and P-variant have different performance in inviscid hypersonic flow past a circular cylinder under structured mesh and the Osher scheme with O-variant can not result in a converged solution. However, detail comparisons of the two fluxes and the treatment of instability have not been investigated yet, which is the motivation of this paper.

The purpose of this paper is to compare the performance of the Osher-O and Osher-P fluxes for the two-dimensional (2D) Euler equation and to improve their shock robustness. Firstly, the Osher flux is combined with first-order and second-order reconstructions, respectively, to construct finite volume methods. Secondly, for inviscid hypersonic flow past a circular cylinder, the Osher schemes are investigated from the aspects of different grids and different Mach numbers. We find that the first-order Osher scheme will produce a "carbuncle" shock or "dislocation" shock and the second-order Osher scheme becomes unstable at the head of the cylinder. In order to improve the robustness of the above numerical methods, we propose an entropy fix technique, which adds dissipation based on the maximum difference of the characteristic speeds across the four interfaces.

https://doi.org/10.4208/aamm.2014.m469 Published online by Cambridge University Press

Numerical results show its effectiveness. We also tested the influence of grid aspect ratio, relative shock position to grid and Mach number on shock instability. Thirdly, to test the influence of the entropy fix on contact resolution and boundary layer resolution, Osher schemes with entropy fix are applied to simulate viscous heating problem and double Mach reflection problem.

The rest of the paper is organized as follows. In Section 2, we state the finite volume discretization with a second-order upwind linear reconstruction and the Osher flux. In Section 3, we present numerical investigations to show the performance of the Osher flux. Moreover, in order to improve the numerical results an entropy fix technique is proposed, which is the most important contribution of this paper. Finally, conclusions drawn from the results are given in Section 4.

2 Finite volume discretization

The 2D Euler equation can expressed as the following conservation form:

$$U_t+f(U)_x+g(U)_y=0, \tag{2.1}$$

where U is the vector of conserved variable, f and g are convective fluxes

$$U=\begin{pmatrix}\rho\\ \rho u\\ \rho v\\ e\end{pmatrix},\quad f(U)=\begin{pmatrix}\rho u\\ \rho u^2+p\\ \rho uv\\ u(e+p)\end{pmatrix},\quad g(U)=\begin{pmatrix}\rho v\\ \rho uv\\ \rho v^2+p\\ v(e+p)\end{pmatrix}.$$

Here ρ, u and v denotes the density, velocity components in x and y directions, respectively, p is the pressure and e is the total energy. For the finite volume method, let us integrate the 2D Euler equation in a finite volume cell Ω_i. Then by using the Green formula, we obtain

$$\frac{\partial\overline{U_i}}{\partial t}+\frac{1}{|\Omega_i|}\int_{\partial\Omega_i}\overrightarrow{F}\cdot\overrightarrow{n}\,dl=0, \tag{2.2}$$

where $\overrightarrow{F}=(f,g)$, $\overline{U_i}=\frac{1}{|\Omega_i|}\int_{\Omega_i}U dxdy$ denotes cell average of U over the cell Ω_i, $|\Omega_i|$ is the area of the cell Ω_i, $\partial\Omega_i$ the boundary of Ω_i, and $\overrightarrow{n}$ the outward unit normal. Here "$\cdot$" represents the inner product algorithm. Suppose the cell Ω_i has m edges. Then the integral of the flux in the second term of Eq. (2.2) can be evaluated as

$$\int_{\partial\Omega_i}\overrightarrow{F}\cdot\overrightarrow{n}\,dl=\sum_{j=1}^{m}h_{ij}(U_{ij,L},U_{ij,R})l_{ij}, \tag{2.3}$$

where h_{ij} is a numerical approximation of $\overrightarrow{F}\cdot\overrightarrow{n}$, $U_{ij,L}$ and $U_{ij,R}$ are the left and right Riemann states of the j_{th} edge of $\partial\Omega_i$, respectively, and l_{ij} is the length of the j_{th} edge. Here $U_{ij,L}$ and $U_{ij,R}$ can be evaluated by reconstruction functions. In the following sections, we

https://doi.org/10.4208/aamm.2014.m469 Published online by Cambridge University Press

will present an upwind limited linear reconstruction procedure and introduce the Osher flux. Then, we finally construct a second order finite volume method by combining the Osher flux and the reconstruction.

2.1 Reconstruction

In this paper, we will consider a constant reconstruction and a linear reconstruction. In a constant reconstruction, the values at any points in the cell are equal to the cell average values. The linear reconstruction is given in the following.

Let us set a finite volume cell Ω to be a triangle $\triangle_{A_1A_2A_3}$ with three vertices A_1, A_2 and A_3. And take u as an example to illustrate the reconstruction procedure. Now consider a linear reconstruction function in $\triangle_{A_1A_2A_3}$ with the form

$$u(X)=\overline{u}_{A_1A_2A_3}+\nabla u_{A_1A_2A_3}\cdot(X-X_{A_1A_2A_3}), \tag{2.4}$$

where $\overline{u}_{A_1A_2A_3}$ is the cell average of u on $\triangle_{A_1A_2A_3}$, and $\nabla u_{A_1A_2A_3}$ the gradient of u at the cell center $X_{A_1A_2A_3}$, evaluated as

$$\nabla u_{A_1A_2A_3}\approx\frac{1}{|\Omega|}\oint_{\partial\Omega}u\overrightarrow{n}dl. \tag{2.5}$$

Firstly, the values at each vertex is reconstructed by using the nodal averaging procedure [25], that is

$$u_{A_i}=\frac{\sum_{j=1}^{N}u_{i,j}/r_{i,j}}{\sum_{j=1}^{N}1/r_{i,j}}, \tag{2.6}$$

where N denotes the number of cells which share the vertex A_i, $u_{i,j}$ is the cell average of u on the j_{th} cell, and $r_{i,j}$ the distance between the cell center of the j_{th} cell and the vertex A_i. Then, the gradient $\nabla u_{A_1A_2A_3}$ can be given by the midpoint-trapezoidal rule, i.e.,

$$\nabla u_{A_1A_2A_3}\approx\frac{1}{|\Omega|}\left(\frac{u_{A_1}+u_{A_2}}{2}l_{12}\overrightarrow{n}_{12}+\frac{u_{A_2}+u_{A_3}}{2}l_{23}\overrightarrow{n}_{23}+\frac{u_{A_3}+u_{A_1}}{2}l_{31}\overrightarrow{n}_{31}\right). \tag{2.7}$$

From [25] we know that the above reconstruction has upwind properties.

Secondly, the reconstruction values $\widetilde{u}_{A_i}$ at the vertex A_i is obtained by substituting Eq. (2.7) into Eq. (2.4) and setting $X=X_{A_i}$. To avoid numerical oscillations, a slope limiter is necessary in the reconstruction procedure. Here to make the reconstruction function to be monotonous, we use the following slope limiter

$$\phi_{A_i}=\begin{cases}\min\left\{1,\dfrac{u_{\max}-\overline{u}_{A_1A_2A_3}}{\widetilde{u}_{A_i}-\overline{u}_{A_1A_2A_3}}\right\}, & \widetilde{u}_{A_i}-\overline{u}_{A_1A_2A_3}>0,\\ \min\left\{1,\dfrac{u_{\min}-\overline{u}_{A_1A_2A_3}}{\widetilde{u}_{A_i}-\overline{u}_{A_1A_2A_3}}\right\}, & \widetilde{u}_{A_i}-\overline{u}_{A_1A_2A_3}<0,\\ 1, & \widetilde{u}_{A_i}-\overline{u}_{A_1A_2A_3}=0,\end{cases} \tag{2.8}$$

https://doi.org/10.4208/aamm.2014.m469 Published online by Cambridge University Press

which is a generalization from the van Leer's 1D limiter [26,27] to 2D unstructured mesh. Here $u_{\min}$ and $u_{\max}$ are the minimum and the maximum of the cell averages surrounding the vertex A_i, respectively.

Finally, the linear reconstruction function with limiter reads

$$u(X)=\overline{u}_{A_1A_2A_3}+\phi_{A_1A_2A_3}\nabla u_{A_1A_2A_3}\cdot(X-X_{A_1A_2A_3}), \tag{2.9}$$

where $\phi_{A_1A_2A_3}=\min_{i=1,2,3}\{\phi_{A_i}\}$.

2.2 Osher flux

For an arbitrary edge noted as AB of the finite volume cell Ω, let us denote the outward normal vector of the edge as $\overrightarrow{n}=(n_x,n_y)$, and the complex flux as $F(U)=(f,g)\cdot\overrightarrow{n}=f(U)n_x+g(U)n_y$. To simplify the question, we take a coordinate transformation as follws,

$$\begin{pmatrix}\xi\\ \eta\end{pmatrix}=\begin{pmatrix}xn_x+yn_y\\ yn_x-xn_y\end{pmatrix}. \tag{2.10}$$

After transformation, the outward nornal vector of the edge becomes $\overrightarrow{n_2}=(1,0)$ in the (ξ,η) coordinate system. In addition, the Euler equation (2.1) can be rewritten as

$$U_t+\widetilde{f}_\xi+\widetilde{g}_\eta=0, \tag{2.11}$$

where $\widetilde{f}=\xi_x f(U)+\xi_y g(U)$ and $\widetilde{g}=\eta_x f(U)+\eta_y g(U)$. According to the transformation (2.10), we have $\xi_x=n_x$ and $\xi_y=n_y$, thus $\widetilde{f}=F(U)$. Now the main task is to compute $\widetilde{f}$ along the edge. If we walk along the boundary $\partial\Omega$ anticlockwise, the inside of the cell is on the left and the outside of the cell is on the right. Assume the left state to be U_L and the right state be U_R. Then it can be treated as a Riemann problem in the ξ direction with flux function $\widetilde{f}$. Hence the one-dimensional Osher flux can be used here. In the following we just present the essential steps of the implementation of Osher flux. We refer the interested readers to [4,22,28] for more details.

The Jacobian matrix of the complex flux is

$$\frac{\partial F(U)}{\partial U}=n_x\frac{\partial f(U)}{\partial U}+n_y\frac{\partial g(U)}{\partial U}, \tag{2.12}$$

which has eigenvalues $\lambda_1=\widetilde{u}\mp c$, $\lambda_2=\widetilde{u}$ and $\lambda_3=\widetilde{u}\pm c$. Here the upper and lower signs are used for the O- and P-variants, respectively. It is referred to as the O-variant when the eigenvalues λ_3, λ_2 and λ_1 are in decreasing order, and as the P-variant when they are in increasing order. The two independent contravariant velocities for the Jacobian matrix are $\widetilde{u}=un_x+vn_y$ and $\widetilde{v}=vn_x-un_y$, respectively. Set Γ_1, Γ_2, Γ_3 be the integral curves corresponding to λ_3, λ_2, λ_1. The Riemann invariants corresponding to $\widetilde{u}-c$ are $\widetilde{u}+\frac{2}{\gamma-1}c$, p/ρ^γ and $\widetilde{v}$. As for $\widetilde{u}+c$, the Riemann invariants are $\widetilde{u}-\frac{2}{\gamma-1}c$, p/ρ^γ and $\widetilde{v}$. As for $\widetilde{u}$, the Riemann invariants are $\widetilde{u}$ and p. Let the two intermediate states be $U_{1/3}=$

https://doi.org/10.4208/aamm.2014.m469 Published online by Cambridge University Press

$(\rho_{1/3},u_{1/3},v_{1/3},p_{1/3})$ and $U_{2/3}=(\rho_{2/3},u_{2/3},v_{2/3},p_{2/3})$, which can be determined by solving the following equations,

$$\rho_{2/3}=\left\{\frac{(\gamma-1)(\widetilde{u}_R-\widetilde{u}_L)/2\pm(c_R+c_L)}{c_R\left[1+(p_L/p_R)^{1/(2\gamma)}(\rho_L/\rho_R)^{-1/2}\right]}\right\}^{\frac{2}{\gamma-1}}\rho_R, \tag{2.13a}$$

$$\rho_{1/3}=\left\{\frac{(\gamma-1)(\widetilde{u}_R-\widetilde{u}_L)/2\pm(c_R+c_L)}{c_L\left[1+(p_R/p_L)^{1/(2\gamma)}(\rho_R/\rho_L)^{-1/2}\right]}\right\}^{\frac{2}{\gamma-1}}\rho_L, \tag{2.13b}$$

$$p_{1/3}=p_L\left(\frac{\rho_{1/3}}{\rho_L}\right)^{\gamma},\quad c_{1/3}=\sqrt{\frac{\gamma p_{1/3}}{\rho_{1/3}}},\quad c_{2/3}=\sqrt{\frac{\gamma p_{2/3}}{\rho_{2/3}}},\quad \widetilde{u}_{1/3}=\widetilde{u}_L\mp\frac{2}{\gamma-1}(c_L-c_{1/3}), \tag{2.13c}$$

$$p_{2/3}=p_{1/3},\qquad \widetilde{u}_{2/3}=\widetilde{u}_{1/3},\qquad \widetilde{v}_{2/3}=\widetilde{v}_R,\qquad \widetilde{v}_{1/3}=\widetilde{v}_L. \tag{2.13d}$$

Then $u_{1/3}$ and $v_{1/3}$ can be obtained from $\widetilde{u}_{1/3}$ and $\widetilde{v}_{1/3}$. Similarly, $u_{2/3}$, $v_{2/3}$ can be obtained from $\widetilde{u}_{2/3}$, $\widetilde{v}_{2/3}$. Thus, $U_{1/3}$ and $U_{2/3}$ are determined.

For the integral curves Γ_1 and Γ_3, we calculate the sonic points $U_{s_1}=(\rho_{s_1},u_{s_1},v_{s_1},p_{s_1})$ and $U_{s_2}=(\rho_{s_2},u_{s_2},v_{s_2},p_{s_2})$, which are determined by the following equations

$$\widetilde{u}_{s_1}=\frac{\gamma-1}{\gamma+1}\widetilde{u}_L\mp\frac{2}{\gamma+1}c_L,\qquad c_{s_1}=\mp\widetilde{u}_{s_1}, \tag{2.14a}$$

$$\rho_{s_1}=\left(\frac{c_{s_1}}{c_L}\right)^{2/(\gamma-1)}\rho_L,\qquad p_{s_1}=p_L\left(\frac{\rho_{s_1}}{\rho_L}\right)^{\gamma}, \tag{2.14b}$$

$$\widetilde{v}_{s_1}=\widetilde{v}_L,\qquad \widetilde{u}_{s_2}=\frac{\gamma-1}{\gamma+1}\widetilde{u}_R\pm\frac{2}{\gamma+1}c_R, \tag{2.14c}$$

$$c_{s_2}=\pm\widetilde{u}_{s_2},\qquad \rho_{s_2}=\left(\frac{c_{s_2}}{c_R}\right)^{2/(\gamma-1)}\rho_R, \tag{2.14d}$$

$$p_{s_2}=p_R\left(\frac{\rho_{s_2}}{\rho_R}\right)^{\gamma},\qquad \widetilde{v}_{s_2}=\widetilde{v}_R. \tag{2.14e}$$

Finally, the Osher flux approximation to the complex flux F is

$$\begin{aligned}
&\frac{1}{2}\left[F(U_L)+F(U_R)-\int_{U_L}^{U_R}|\partial_U F(U)|dU\right]\\
=&\frac{1}{2}[1+\mathrm{sign}(\lambda_3(U_0))]F_0+\frac{1}{2}[\mathrm{sign}(\lambda_3(U_{1/3}))-\mathrm{sign}(\lambda_3(U_0))]F_{s_1}\\
&+\frac{1}{2}[\mathrm{sign}(\widetilde{u}_{1/3})-\mathrm{sign}(\lambda_3(U_{1/3}))]F_{1/3}+\frac{1}{2}[\mathrm{sign}(\lambda_1(U_{2/3}))-\mathrm{sign}(\widetilde{u}_{1/3})]F_{2/3}\\
&+\frac{1}{2}[\mathrm{sign}(\lambda_1(U_1))-\mathrm{sign}(\lambda_1(U_{2/3}))]F_{s_2}+\frac{1}{2}[1-\mathrm{sign}(\lambda_1(U_1))]F_1,
\end{aligned} \tag{2.15}$$

where $F_{s_1}=F(U_{s_1})$, $F_0=F(U_L)$. Since the intermediate states $U_{1/3}$ and $U_{2/3}$ are different for O-variant and P-variant, the resulted flux are different, which will be verified by numerical investigation in Section 3.

https://doi.org/10.4208/aamm.2014.m469 Published online by Cambridge University Press

2.3 Osher flux with entropy fix

In this subsection, we give small perturbation analysis for Osher-O flux and Osher-P flux to explain instabilities of such fluxes. Then we propose an entropy fix technique to improve the robustness of Osher flux.

2.3.1 Small perturbation analysis

We assume initial values at two adjacent cells

$$\begin{aligned} &\rho_L=1-\hat{\rho}, && u_L=u_0-\hat{u}, && v_L=0, && p_L=1-\hat{p},\\ &\rho_R=1+\hat{\rho}, && u_R=u_0+\hat{u}, && v_R=0, && p_R=1+\hat{p}, \end{aligned}$$

as shown in Fig. 1. Since perturbations $\hat{\rho}$, $\hat{u}$, $\hat{p}$ are small, we can obtain

$$c_L=\sqrt{\gamma}\Big(1-\frac{\hat{p}}{2}+\frac{\hat{\rho}}{2}\Big),\quad c_R=\sqrt{\gamma}\Big(1+\frac{\hat{p}}{2}-\frac{\hat{\rho}}{2}\Big),$$

and the two intermediate states

$$\begin{aligned} &\rho_{1/3}=\Big(1-\hat{\rho}+\frac{\hat{p}}{\gamma}\Big), && u_{1/3}=u_0-\hat{u}, && v_{1/3}=v_{2/3}=\frac{\hat{p}}{\sqrt{\gamma}}, && c_{1/3}=\sqrt{\gamma}\Big(1+\frac{\hat{\rho}}{2}-\frac{\hat{p}}{2\gamma}\Big),\\ &\rho_{2/3}=\Big(1+\hat{\rho}-\frac{\hat{p}}{\gamma}\Big), && u_{2/3}=u_0+\hat{u}, && p_{2/3}=p_{1/3}=1, && c_{2/3}=\sqrt{\gamma}\Big(1-\frac{\hat{\rho}}{2}+\frac{\hat{p}}{2\gamma}\Big). \end{aligned}$$

Thus the fluxes can be evaluated as

$$F(U_{1/3})=F(U_{2/3})=\begin{pmatrix} -\frac{\hat{p}}{\sqrt{\gamma}}\\ -u_0\frac{\hat{p}}{\sqrt{\gamma}}\\ -1\\ -\Big(\frac{\gamma}{\gamma-1}+\frac{u_0^2}{2}\Big)\frac{\hat{p}}{\sqrt{\gamma}} \end{pmatrix},\quad F(U_L)=F(U_R)=\begin{pmatrix} 0\\ 0\\ -1\\ 0 \end{pmatrix}.$$

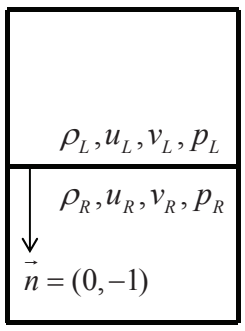


Figure 1: Initial values with small perturbation.

https://doi.org/10.4208/aamm.2014.m469 Published online by Cambridge University Press

Finally, the Osher-P flux is

$$\frac{1}{2}\{F(U_L)+F(U_R)-[(F(U_L)-F(U_{1/3}))+(F(U_R)-F(U_{2/3}))]\}$$

$$=\frac{1}{2}(F(U_{1/3})+F(U_{2/3}))=\begin{pmatrix} -\frac{\hat{p}}{\sqrt{\gamma}} \\ -u_0\frac{\hat{p}}{\sqrt{\gamma}} \\ -1 \\ -\left(\frac{\gamma}{\gamma-1}+\frac{u_0^2}{2}\right)\frac{\hat{p}}{\sqrt{\gamma}} \end{pmatrix}$$

and Osher-O flux is

$$\frac{1}{2}\{F(U_L)+F(U_R)-[(F(U_{1/3})-F(U_L))+(F(U_{2/3})-F(U_R))]\}$$

$$=F(U_L)+F(U_R)-\frac{1}{2}(F(U_{1/3})+F(U_{2/3}))=\begin{pmatrix} \frac{\hat{p}}{\sqrt{\gamma}} \\ u_0\frac{\hat{p}}{\sqrt{\gamma}} \\ -1 \\ \left(\frac{\gamma}{\gamma-1}+\frac{u_0^2}{2}\right)\frac{\hat{p}}{\sqrt{\gamma}} \end{pmatrix}.$$

We can see that both the Osher-P flux and the Osher-O flux are only affected by the pressure perturbation ($\hat{p}\neq 0$) but not affected by density or shear velocity perturbations ($\hat{\rho}\neq 0$, $\hat{u}\neq 0$). According to the work of Pandolfi in [20], such kind of fluxes are strongly affected by numerical instabilities and adding appropriate dissipation is a good technique to deal with this problem.

2.3.2 Entropy fix

We propose entropy fix technique for the interface face0, as shown in Fig. 2. It is based on a detection routine as in [20]. Here the maximum difference of the characteristic speeds across the four interfaces connected to the interface face0 is evaluated by U_L and U_R directly but not by the intermediate states,

$$\eta=\max\{\epsilon_i\}_{i=1,2,3,4},\quad \epsilon_i=|\widetilde{u}_i^L-\widetilde{u}_i^R|+|c_i^L-c_i^R|, \tag{2.16}$$

where $\widetilde{u}_i=un_x+vn_y$ is the velocity components normal to the interface face$i$. Then the global flux F_{ef} across the interface face0 is evaluated as

$$F_{ef}=F_{Osher}-\eta(U_0^R-U_0^L),$$

where U_0^R and U_0^L are the reconstructed variables at the interface face0. Here F_{Osher} is the Osher flux computed by (2.15). The entropy fix is added for original Osher flux F_{Osher} but not the intermediate flux $F_{1/3}$ or $F_{2/3}$.

https://doi.org/10.4208/aamm.2014.m469 Published online by Cambridge University Press

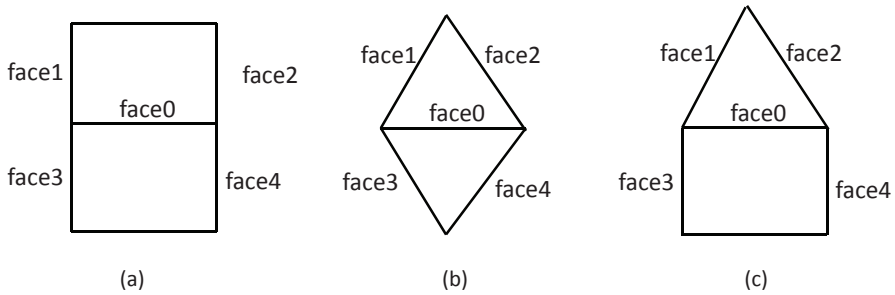


Figure 2: Four interfaces connected to the interface face0.

2.4 Boundary conditions

For the side at the solid boundary of the computational area, we take the physical solid wall boundary condition. Denote the cell average value of the cell containing this side as $U_{1/2}$. Then we can find the boundary value U_0 by using the integral curve of $\widetilde{u}-c$ which connects $U_{1/2}$ to U_0. And U_0 is calculated according to the Riemann invariants

$$\frac{2}{\gamma-1}c_0=\widetilde{u}_{1/2}+\frac{2}{\gamma-1}c_{1/2}, \tag{2.17a}$$

$$\widetilde{u}_0=0, \tag{2.17b}$$

$$\frac{p_0}{\rho_0^\gamma}=\frac{p_{1/2}}{\rho_{1/2}^\gamma}, \tag{2.17c}$$

$$\widetilde{v}_0=\widetilde{v}_{1/2}. \tag{2.17d}$$

Hence c_0 is simply determined by Eq. (2.17a). By noting that $c_0=\sqrt{\gamma p_0/\rho_0}$, it is straight forward to solve from Eq. (2.17c) that

$$\rho_0=\left(\frac{c_0}{c_{1/2}}\right)^{\frac{2}{\gamma-1}}\rho_{1/2},\quad p_0=\left(\frac{\rho_0}{\rho_{1/2}}\right)^{\gamma}p_{1/2}. \tag{2.18}$$

Therefore, the values of U_0 are determined. If a sonic point exists in the integral curve of $\widetilde{u}-c$, which denoted by $U_{1/6}$, then the corresponding state can be obtained from Riemann invariants, i.e.,

$$\widetilde{u}_{1/6}=c_{1/6}=\frac{\gamma-1}{\gamma+1}\left(\widetilde{u}_{1/2}+\frac{2}{\gamma-1}c_{1/2}\right),\qquad \rho_{1/6}=\left(\frac{c_{1/6}}{c_{1/2}}\right)^{\frac{2}{\gamma-1}}\rho_{1/2}, \tag{2.19a}$$

$$p_{1/6}=\left(\frac{\rho_{1/6}}{\rho_{1/2}}\right)^{\gamma}p_{1/2},\qquad \widetilde{v}_{1/6}=\widetilde{v}_{1/2}. \tag{2.19b}$$

So we have

$$\int_{U_{1/2}}^{U_0}(\partial F)^- dU=\begin{cases} F(U_0)-F(U_{1/6}), & \widetilde{u}_{1/2}-c_{1/2}>0,\\ F(U_0)-F(U_{1/2}), & \widetilde{u}_{1/2}-c_{1/2}\le 0, \end{cases} \tag{2.20}$$

https://doi.org/10.4208/aamm.2014.m469 Published online by Cambridge University Press

and

$$\int_{U_{1/2}}^{U_0}(\partial F)^+ dU=\begin{cases} F(U_{1/6})-F(U_{1/2}), & \widetilde{u}_{1/2}-c_{1/2}>0,\\ 0, & \widetilde{u}_{1/2}-c_{1/2}\leq 0.\end{cases} \tag{2.21}$$

Therefore, the Osher flux for the solid boundary is

$$\frac{1}{2}\Big[F(U_{1/2})+F(U_0)-\int_{U_{1/2}}^{U_0}|\partial F|dU\Big]=\begin{cases} F_0+F_{1/2}-F_{1/6}, & \widetilde{u}_{1/2}-c_{1/2}>0,\\ F_0, & \widetilde{u}_{1/2}-c_{1/2}\leq 0.\end{cases} \tag{2.22}$$

2.5 Time discretization

We take TVD Runge-Kutta scheme for time discretization, i.e.,

$$U^{(1)}=U^n+\Delta t L(U^n), \tag{2.23a}$$

$$U^{n+1}=\frac{U^n}{2}+\frac{1}{2}\big[U^{(1)}+\Delta t L\big(U^{(1)}\big)\big], \tag{2.23b}$$

where Δt is the time-step. In this paper we choose $\Delta t=\frac{CFl\cdot\Delta x}{\max\{|u|+c,|v|+c\}}$ for Euler equations, where Δx is the space-step and $CFL=0.1$ is fixed for convenience.

3 Numerical investigation

3.1 Inviscid hypersonic flow past a circular cylinder

We present in this section numerical experiments for inviscid hypersonic flow past a circular cylinder. We consider different grid aspect ratios, different relative shock positions to the grid and different Mach numbers.

We mainly consider three grids with different grid density, which are the grids with 40×80 (Grid1) intervals, 30×240 intervals (Grid2) and 87×100 intervals (Grid3), as shown in Fig. 3. Here the grid with 40×80 intervals, for instance, means that it is composed of 40 radials and 80 tangential intervals. In addition, grid points on the boundary are equally located for Grid1.

The numerical results are categorized according to three properties which are symmetry, convergence and shock location. We use "1" and "0" to denote the good performance and bad performance of the property as shown in Table 1. Solution is convergent if the density residual $Res^n=\max(|\rho^n-\rho^{n-1}|)$ reduces by at least fifth orders of magnitude. To evaluate the quality of the numerical solution, we divide the 8 results into three classes, which contains good results with symmetric convergent solution marked by black (class A), bad results with shock breakdown marked by red (class B) and the other results marked by blue (class C), as shown in Table 2.

Firstly, we apply first order and second order schemes based on Osher-O and Osher-P to solve the problem on the three grids for the case $M_\infty=20$. The numerical results are given in Table 3 and the results on Grid1 are also shown in Fig. 4. We can see that first-order Osher-O scheme, second-order Osher-O and second-order Osher-P scheme yield

https://doi.org/10.4208/aamm.2014.m469 Published online by Cambridge University Press

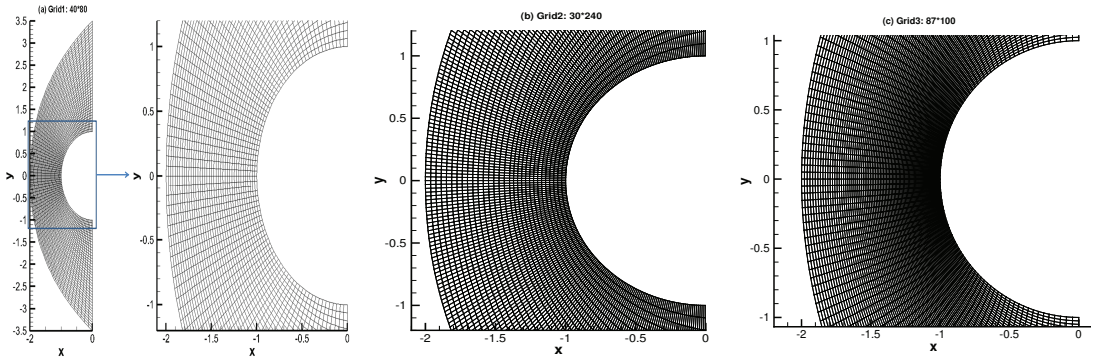


Figure 3: Grid1, Grid2 and Grid3.

"carbuncle" shocks at the head of cylinder and the first-order Osher-P scheme yields a "dislocation" shock at the angle $\theta \approx 45^0$ near the bow shock. After entropy fix technique in Section 2.3.2 is taken, all of the four schemes result in convergent solutions and are free from "carbuncle" shock or "dislocation" shock. These results show the effectiveness of the entropy fix technique. As for Roe flux with Harten's entropy fix, from Table 3 we can see that convergent solutions on these three grids can only be obtained by first order schemes.

Table 1: Three properties of the numerical solution.

Shock location	Symmetry	Convergence
1: regular	1: symmetric	1: convergent
0: breakdown	0: asymmetric	0: not convergent

Table 2: Quality evaluation of the numerical solution.

Classes	A	B			C			
Case	7	6	5	4	3	2	1	0
Solution	1,1,1	1,1,0	1,0,1	1,0,0	0,1,1	0,1,0	0,0,1	0,0,0

Table 3: Test results for different numerical fluxes on grids with different grid ratio ($M_\infty = 20$).

Schemes	Grid1	Grid2	Grid3
1st Osher-O	0	0	0
1st Osher-P	3	3	3
1st Osher-O(E-fix)	7	7	7
1st Osher-P(E-fix)	7	7	7
1st Roe(E-fix)	7	7	7
2nd Osher-O	0	0	0
2nd Osher-P	2	3	4
2nd Osher-O(E-fix)	7	7	7
2nd Osher-P(E-fix)	7	7	7
2nd Roe(E-fix)	0	0	0

https://doi.org/10.4208/aamm.2014.m469 Published online by Cambridge University Press

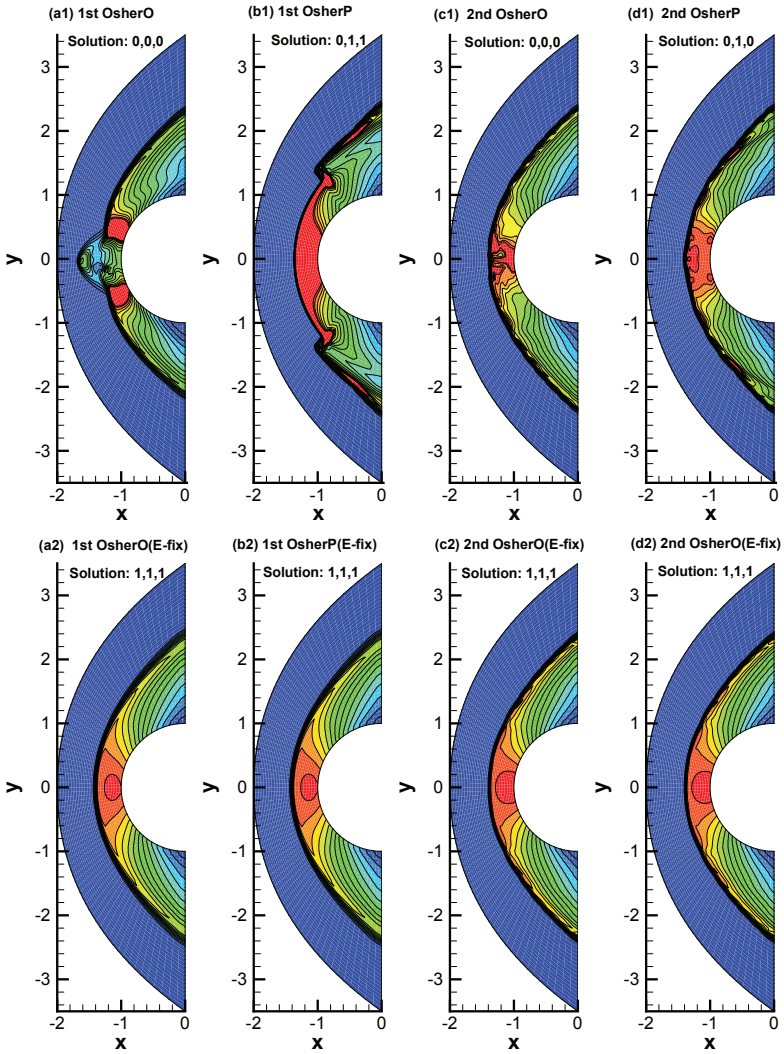


Figure 4: Density contours for schemes without entropy fix (Up) and with entropy fix (Down) on Grid1.

Secondly, we investigate the influence of grid aspect ratio, relative shock position to the grid (shock-grid-position) and Mach number on shock stability. Using the Grid1, we can obtain grids with different aspect ratio by refining tangential intervals and can obtain a series of grids with different shock-grid-position by moving the middle 11 grid points in the symmetric line towards the head of the cylinder with distances $\alpha\cdot\Delta x$ ($\alpha=$ 0.0,0.1,0.2,$\cdots$,1.0), as shown in Fig. 5. Tables 4 and 5 give numerical results for $M_\infty=20$ while Table 6 gives the numerical results for the case $M_\infty=8$. For the flux with entropy fix, shock stability are mainly influenced by grid aspect ratio for first order schemes but mainly by shock-grid-position and Mach number for second order schemes. The different performance between first order scheme and second order scheme reveal that reconstruc-

https://doi.org/10.4208/aamm.2014.m469 Published online by Cambridge University Press

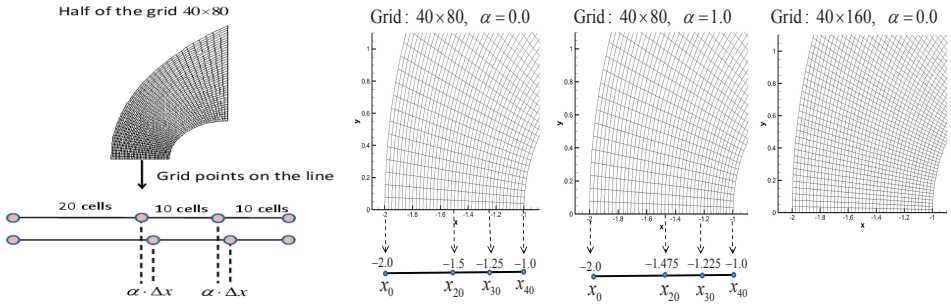


Figure 5: Grid generation based on Grid1.

tion function together with the slope limiter also affect dissipation properties of the final schemes and thus influence shock stability.

Compare the results in Table 5 and Table 6, we can see that the first-order Osher-P scheme converges to smooth solutions on 7 grids for $M_\infty=8$ but results in a "dislocation" shock as shown in Fig. 4(b1) on 6 grids for $M_\infty=20$. Mach number has influence on shock stability of first-order Osher-P scheme. However, first-order Osher-O schemes can always yields a "carbuncle" shock for both $M_\infty=8$ and $M_\infty=20$. For second order schemes, both Osher-P and Osher-O can not obtain correct solutions. In fact, Osher-P and Osher-O has different performances. After using entropy fix technique, the numerical results are improved. For Osher-O (E-fix) and Osher-P (E-fix), first order schemes can obtain good results in most grids and second order schemes can obtain correct convergent results on three grids ($\alpha=0.0$, 0.1 and 0.2 for the case $M_\infty=20$; $\alpha=0.0$, 0.8 and 0.9 for the case $M_\infty=8$). Second order Osher-O (E-fix) and Osher-P (E-fix) has similar numerical performances. Thus, the entropy fix largely improve the robustness of Osher-O flux and Osher-P flux. For Roe flux, numerical results of first order schemes has similar performance like Osher flux, but the second order Roe scheme yields carbuncle on many grids. Thus, Osher-O (E-fix) flux and Osher-P (E-fix) flux may be more robust than Roe (E-fix).

We also apply our entropy fix technique on the original Roe flux and call this resultant

Table 4: Test results for different numerical fluxes on grids with different grid aspect ratio ($M_\infty=20$).

Schemes Grid	40×40	40×80	40×120	40×160	40×200	40×240
1st Osher-O	0	0	0	0	0	0
1st Osher-P	5	3	3	3	3	3
2nd Osher-O	0	0	0	0	0	0
2nd Osher-P	3	2	0	0	0	0
1st Osher-O(E-fix)	5	7	7	7	7	7
1st Osher-P(E-fix)	7	7	7	4	4	6
2nd Osher-O(E-fix)	7	7	7	7	7	7
2nd Osher-P(E-fix)	7	7	7	7	7	7
1st Roe(E-fix)	7	7	4	7	7	7
2nd Roe(E-fix)	2	0	0	0	0	0

https://doi.org/10.4208/aamm.2014.m469 Published online by Cambridge University Press

Table 5: Test results for different numerical fluxes on grids with different shock-grid-position ($M_\infty = 20$).

Schemes Grid (α)	$\alpha = 0.0$	0.1	0.2	0.3	0.4	0.5	0.6	0.7	0.8	0.9	1.0
1st Osher-O	0	0	0	0	0	0	0	0	0	0	0
1st Osher-P	3	3	3	3	3	3	5	4	7	7	7
2nd Osher-O	0	0	0	0	0	0	0	0	0	0	0
2nd Osher-P	2	2	2	1	1	2	0	0	2	2	2
1st Osher-O(E-fix)	7	7	7	7	7	7	7	7	7	7	7
1st Osher-P(E-fix)	7	7	7	7	7	7	7	7	7	7	7
2nd Osher-O(E-fix)	7	7	7	5	5	5	5	5	4	4	5
2nd Osher-P(E-fix)	7	7	7	5	5	5	4	5	4	4	4
1st Roe(E-fix)	7	7	7	7	7	7	7	7	7	5	7
1st Roe(Zhu E-fix)	5	5	5	7	7	7	7	7	5	5	5
1st Roe(HZ E-fix)	7	7	7	7	7	7	7	7	7	7	7
2nd Roe(E-fix)	0	0	7	0	0	5	5	0	0	0	0
2nd Roe(Zhu E-fix)	3	0	4	5	5	5	1	0	2	2	0
2nd Roe(HZ E-fix)	3	2	1	3	5	5	5	4	5	5	5

Table 6: Test results for different numerical fluxes on grids with different shock-grid-position ($M_\infty = 8$).

Schemes	$\alpha = 0.0$	0.1	0.2	0.3	0.4	0.5	0.6	0.7	0.8	0.9	1.0
1st Osher-O	0	0	0	0	0	0	0	0	0	0	0
1st Osher-P	5	7	7	7	7	7	7	5	5	5	7
2nd Osher-O	0	0	0	0	0	0	0	0	0	0	0
2nd Osher-P	5	4	5	4	3	3	2	3	0	5	5
1st Osher-O(E-fix)	7	7	7	7	7	7	7	7	7	7	7
1st Osher-P(E-fix)	7	7	7	7	7	7	7	7	7	7	7
2nd Osher-O(E-fix)	7	4	5	5	5	4	4	4	7	7	5
2nd Osher-P(E-fix)	7	5	5	5	5	4	4	4	7	7	5
1st Roe(E-fix)	7	7	7	7	7	7	4	5	5	7	7
1st Roe(Zhu E-fix)	7	7	7	7	5	5	4	4	5	7	7
1st Roe(HZ E-fix)	7	7	7	7	7	7	7	7	7	7	7
2nd Roe(E-fix)	0	7	5	0	0	2	2	2	0	5	7
2nd Roe(Zhu E-fix)	5	5	7	4	0	0	0	0	1	4	5
2nd Roe(HZ E-fix)	4	5	7	4	0	0	5	6	2	4	5

flux as Roe (Zhu E-fix). From Table 5 and Table 6, we can see that Roe (Zhu E-fix) is not as good as Osher flux with entropy fix. The reason may lies in the difference between the original 1D Roe flux and 1D original Osher flux. Then the fix technique is used for Roe (E-fix) and the resultant Roe (HZ E-fix) performs better than Roe (E-fix) for first order schemes but also can not obtain robust results for second order schemes.

3.2 Viscous heating problems

We consider hypersonic heating on the wall of a two-dimensional blunt body with $r =$ 20mm radius mounted in Nagoya University Shock Tunnel [30], in which the freestream

https://doi.org/10.4208/aamm.2014.m469 Published online by Cambridge University Press

Table 7: Quality evaluation of the numerical solution.

Grid	2nd Osher-O(E-fix)		2nd Osher-P(E-fix)	
	pressure error	heating error	pressure error	heating error
Grid 4: 150×80	1.11%	4.09%	0.79%	3.29%
Grid 5: 150×240	2.37%	3.83%	2.48%	6.12%
Grid 6: 147×100	0.37%	1.34%	0.37%	1.38%
Grid 7: 16242	0.19%	0.46%	0.17%	0.81%

conditions are $M_\infty=8.1$, $P_\infty=370.6$Pa, $Re=1.3\times10^5$, $T_\infty=63.73$K and $T_{wall}=300$K. This problem is also considered by Kitamura in [31,32]. From Table 3 in Section 3.1, we have tested that second order Osher-O (E-fix) and second order Osher-P (E-fix) schemes can obtain correct solutions on Grid1, Grid2 and Grid3. To compute heating, we generate another three grids based on the Grid1, Grid2 and Grid3 by taking grid refinement only near the wall so that the cell Reynolds number is $Re_{cell}=1.3$. The new grids has 150×80 cells (Grid4), 150×240 cells (Grid5) and 147×100 cells (Grid6) correspondingly with local plots shown in Fig. 6.

The derivatives in viscous term are evaluated as

$$\nabla u_L=\nabla u_{GHIJ}=\frac{1}{S_{GHIJ}}\left[u_B l_{GH}\overrightarrow{n}_{GH}+u_N l_{HI}\overrightarrow{n}_{HI}+u_E l_{IJ}\overrightarrow{n}_{IJ}+u_M l_{JG}\overrightarrow{n}_{JG}\right],$$

where u_M and u_N are cell averages, u_B and u_E are values at vertices, as shown in Fig. 13.

Second order schemes based on Osher-O (E-fix), Osher-P (E-fix) and Roe (E-fix) are tested. Pressure distributions are displayed in Fig. 6. We can see that Osher-O (E-fix) and Osher-P (E-fix) obtain similar numerical results and can obtain smooth flowfields. The surface pressure and heating profiles are shown in Fig. 7. Here we use theoretical stagnation pressure $P_{10}/P_\infty=84.9$ and accurate stagnation heating $q_{FR}=17.5\text{W/cm}^2$, which are the same as that in [31,32]. The surface pressure and heating profile are also smooth. It is concluded that both of shock stability and boundary layer resolution are crucial for heating computations in [32]. The errors in resultant pressure and heating for Osher-O (E-fix) and Osher-P (E-fix) on three grids are small as shown in Table 7, which may indicate that Osher flux with entropy fix has good shock stability and good boundary layer resolution. The results on the Grid6 are more accurate than that on the Grid4 and Grid5, which reveal that grid density near shock and grid distribution near the wall will influence pressure distribution and heating profiles. Roe (E-fix) yields carbuncle on Grid4 and Grid5, and shows weak asymmetry in flowfields on Grid6. For all three grids, Roe (E-fix) has obvious asymmetric patterns in surface heating.

3.3 Double Mach reflection

Double Mach reflection problem described in [29] is solved by Osher schemes. Results on a grid with 240×960 intervals at time $t=0.2$ are displayed in Fig. 8. We can see that both first order Osher-O and first order Osher-P yield carbuncle for the principal Mach shock

https://doi.org/10.4208/aamm.2014.m469 Published online by Cambridge University Press

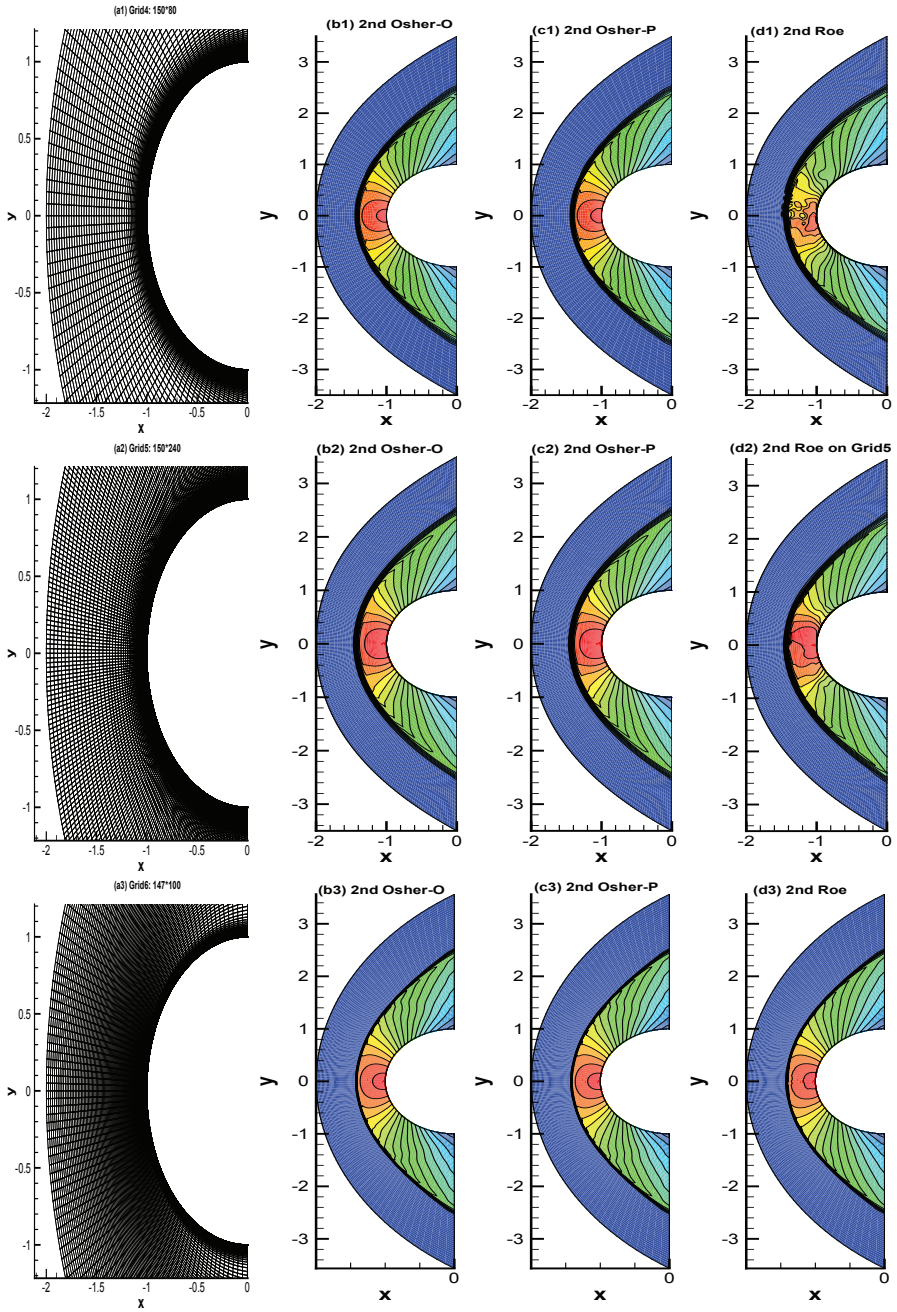


Figure 6: Pressure distributions of schemes with entropy fix on Grid4 (Up), Grid5 (Middle) and Grid6 (Down).

near $x=2.8$, as shown in Figs. 8(a1) and (b1). After taking entropy fix, the carbuncle phenomena disappear, as shown in Figs. 8(a2) and (b2). For second order Osher-O scheme and second order Osher-P scheme, the shape of the principal Mach stem appears to be in-

https://doi.org/10.4208/aamm.2014.m469 Published online by Cambridge University Press

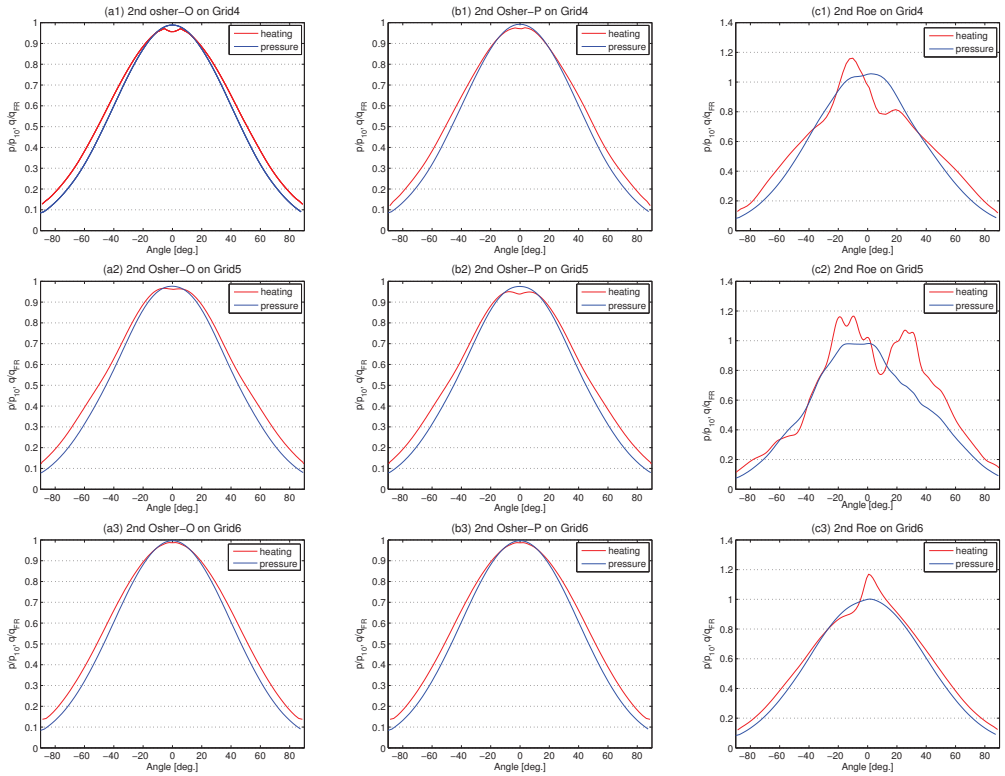


Figure 7: Surface pressure and heating profiles of schemes with entropy fix.

correct and a piece of jet has struck the principle Mach shock, as shown in Figs. 6(c1) and (d1). Second order Osher schemes with entropy fix are free from carbuncle phenomenon.

In order to verify that the entropy fix won't influence the robustness of shock, we give the contour plots of the ratio of the maximum difference η in (2.16) to $\lambda_{\max}=\max\{|\widetilde{u}_L|+c_L,|\widetilde{u}_R|+c_R\}$ for interfaces with $n_x=0$ and $n_y=0$ respectively, as shown in Fig. 9. We can see that near the Mach shock the ratio $\frac{\eta}{\lambda_{\max}}$ is much larger for the interfaces with $n_x=0$ than those with $n_y=0$, which means the entropy fix is mainly given for the interfaces perpendicular to the Mach shock and thus the entropy fix may not influence shock robustness. We also make a test of only taking entropy fix for the interfaces with $n_x=0$. We find that the numerical result is also free from carbuncle phenomenon and is almost the same with the result in Fig. 8(a2). We also show the density distribution along lines $x=2.4$ and $y=0.2$ in Fig. 10. These results indicate that adding appropriate dissipation for the interfaces perpendicular to the shock is the reason for the entropy fix to prevent carbuncle phenomenon.

From Fig. 9, we can see that the ratio is less than 0.1 for contact discontinuity, which means the added dissipation is very small and may not influence contact resolution. Fig. 11 gives comparisons for second order schemes. Entropy fix also did not influence the robustness of the Mach shock. In addition, for contact discontinuity second order

https://doi.org/10.4208/aamm.2014.m469 Published online by Cambridge University Press

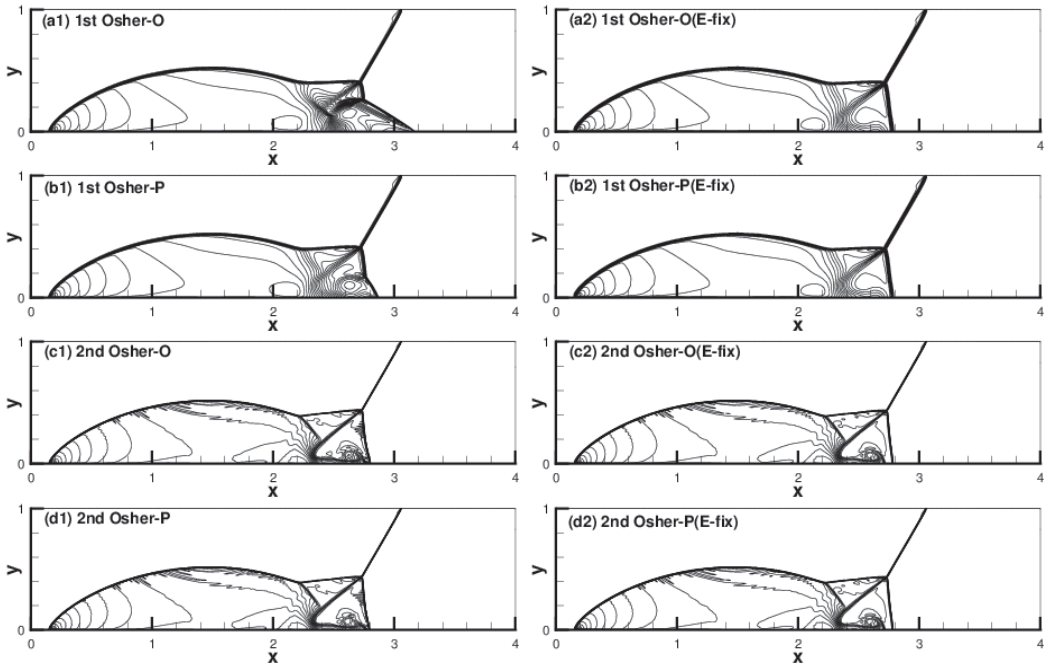


Figure 8: Density distributions at time 0.2 for the double Mach reflection problem.

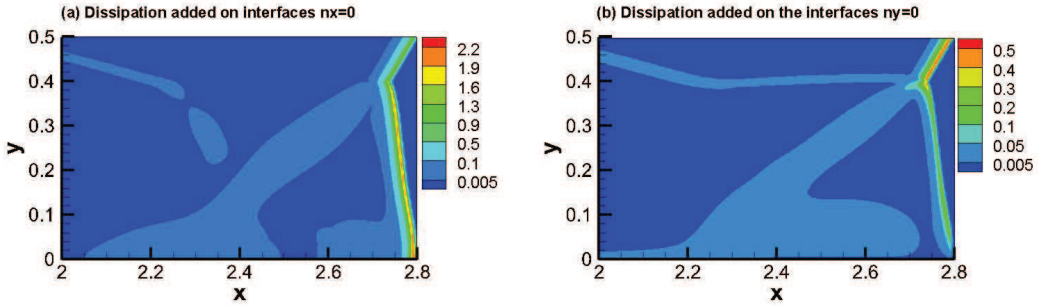


Figure 9: Contour plots of the ratio $\frac{\eta}{\lambda_{\max}}$ for interfaces with $n_x=0$ (left plot) and $n_y=0$ (right plot).

Osher schemes with entropy fix locates between second order Osher schemes without entropy fix and second order schemes with Roe flux.

3.4 Tests on unstructured grids

In this section, we make tests for unstructured grids. Firstly, we generate triangular grids based on a series of quadrilateral grids with different shock-grid-location in Section 3.1, see one such grid in Fig. 12. From Table 8, we can see that the entropy fix also improve the robustness of Osher scheme on triangular grids. Secondly, we recompute the vicous heating problem in Section 3.2 on an unstructured grid. The derivatives at the interfaces

https://doi.org/10.4208/aamm.2014.m469 Published online by Cambridge University Press

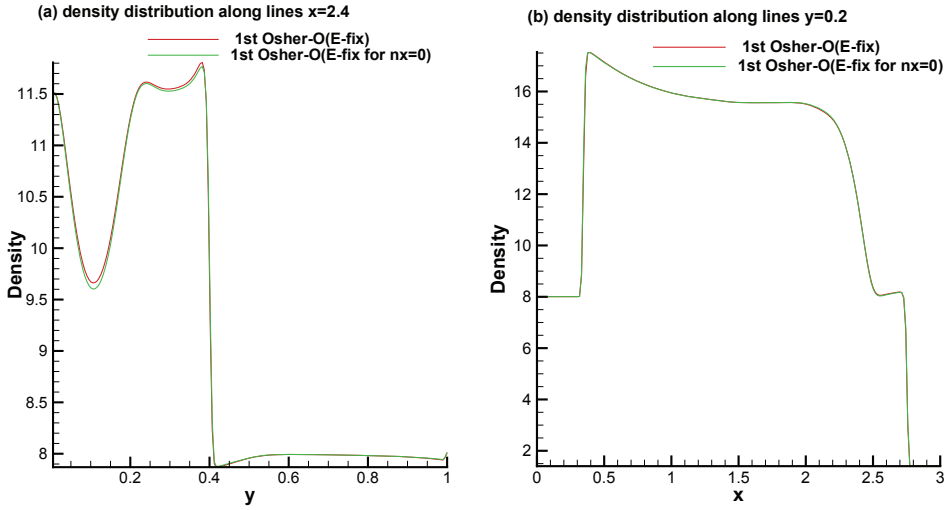


Figure 10: Comparison between Osher-O with entropy fix for all interfaces and only for interfaces with $n_x=0$.

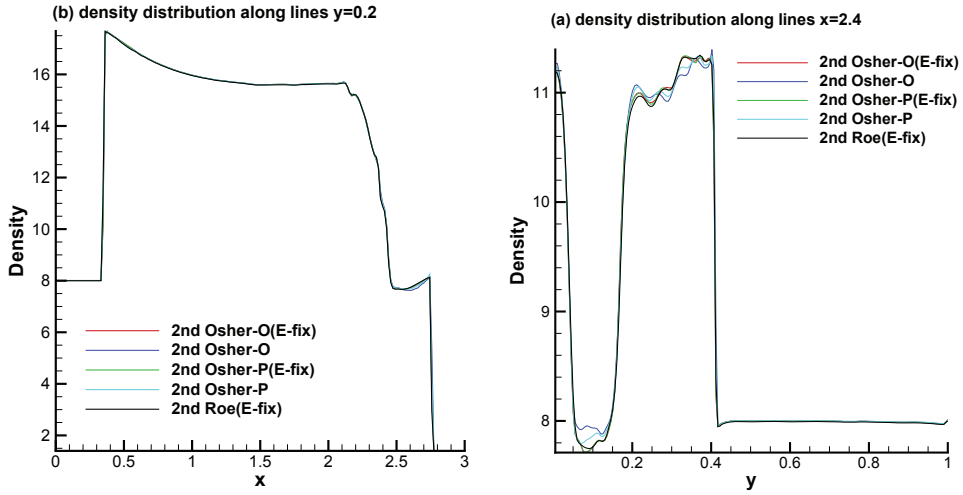


Figure 11: Comparison between second order Osher-O and Osher-P schemes.

in Figs. 13(b) and (c) are evaluated as

$$\nabla u_L=\frac{1}{|S_{MBNE}|}\{u_{MB}l_{MB}\overrightarrow{n}_{MB}+u_{BN}l_{BN}\overrightarrow{n}_{BN}+u_{NE}l_{NE}\overrightarrow{n}_{NE}+u_{EM}l_{EM}\overrightarrow{n}_{EM}\},\qquad(3.1)$$

where $u_{MB}=\frac{u_M+u_B}{2}$, u_M is cell averages, u_B is the value at vertices.

A hybrid grid is generated based on Grid6 by keeping quadrilateral grids in the area near the wall and using triangular grids in the left area, as shown in Fig. 14(a). From Figs. 14(b) and (c), we can see that second order Osher-O (E-fix) and second order Osher-

https://doi.org/10.4208/aamm.2014.m469 Published online by Cambridge University Press

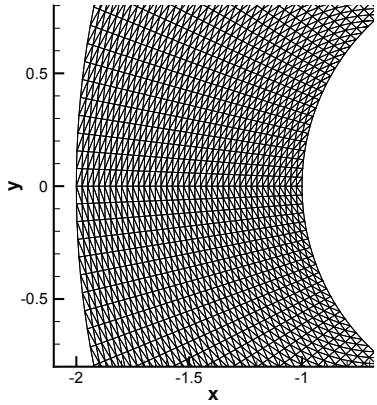


Figure 12: An triangular grid obtained based on the quadrilateral grid with $\alpha = 0.0$.

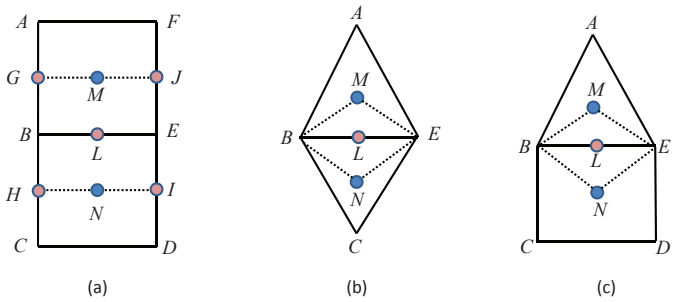


Figure 13: Integral path for computing derivatives in viscous term.

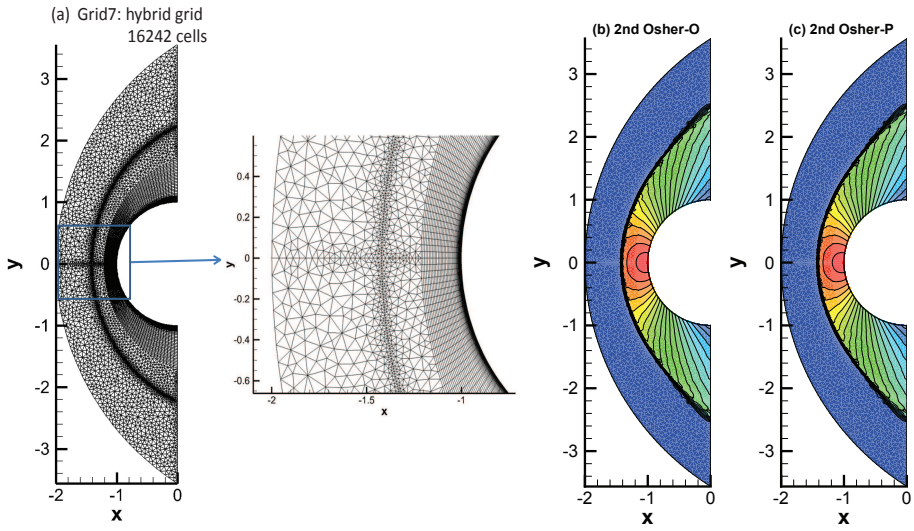


Figure 14: Pressure distributions of schemes with entropy fix on hybrid grid.

https://doi.org/10.4208/aamm.2014.m469 Published online by Cambridge University Press

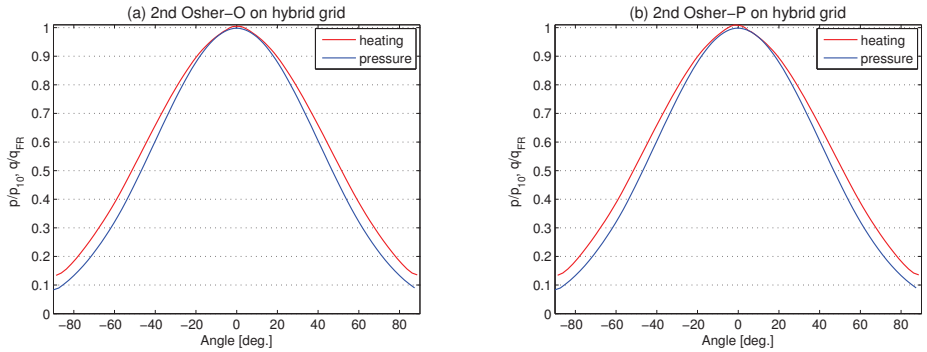


Figure 15: Surface pressure and heating profiles on hybrid grid.

P (E-fix) obtain similar numerical results and can obtain smooth flowfields. In addition, Fig. 15 shows that the surface pressure and heating profile are also smooth. Table 7 also shows that the errors in resultant pressure and heating are small.

Table 8: Test results for Osher fluxes on triangular grids based on quadrilateral grids with different shock-grid-position ($M_\infty = 20$).

Schemes Grid (α)	$\alpha = 0.0$	0.1	0.2	0.3	0.4	0.5	0.6	0.7	0.8	0.9	1.0
1st Osher-O	5	5	5	5	0	0	0	0	0	0	0
1st Osher-P	3	3	3	3	0	3	1	1	1	3	3
1st Osher-O(E-fix)	7	7	7	5	5	5	5	7	7	7	7
1st Osher-P(E-fix)	7	7	7	7	7	7	7	5	7	7	7

4 Conclusions

In this paper we have compared the Osher-O and the Osher-P schemes for the 2D Euler equation and proposed an entropy fix technique to improve their robustness. For an inviscid hypersonic flow past a circular cylinder, it has been shown that the first-order Osher-O scheme based on quadrangular grids always yields a "carbuncle" shock in front of the cylinder and the first-order Osher-P scheme results in a "dislocation" shock for the cases with high Mach number. The second-order Osher schemes will always fail to obtain correct convergent solutions. To improve the robustness of the Osher schemes, we have proposed an entropy fix technique. Numerical tests on a series of grids verify that the first-order Osher schemes with entropy fix can obtain correct convergent solutions for most grids while second order Osher schemes can obtain correct convergent solutions for some grids. Thus, the entropy fix largely improve the robustness of Osher-O flux and Osher-P flux. Numerical results on hypersonic heating on the wall of blunt-body and double Mach reflection show that influence of the added dissipation on boundary-layer resolution and contact resolution is very small. The methods proposed in this paper

https://doi.org/10.4208/aamm.2014.m469 Published online by Cambridge University Press

can be generalized to moving grids by changing the outer normal of each edge at each time step. The future work will involve the shock-robust combination of Osher flux with appropriate slope limiters.

Acknowledgments

H. Zhu was supported by the Natural Science Foundation of China (Grant No. 11301525). We would like to thank Dr. Xinghua Chang for providing some unstructured grids.

References

[1] B. Engquist and S. Osher, *Stable and entropy satisfying approximations for transonic flow calculations,* Math. Comput., 34 (1980), pp. 45–75.
[2] S. Osher and F. Solomon, *Upwind difference schemes for hyperbolic systems of conservation laws*, Math. Comput., 38 (1982), pp. 339–374.
[3] P. Roe, *Approximate Riemann solvers, parameter vectors, and difference schemes*, J. Comput. Phys., 43 (1981), pp. 357–372.
[4] S. Osher and S. Chakravarthy, *Upwind schemes and boundary conditions with applications to Euler equations in general geometries*, J. Comput. Phys., 50 (1983), pp. 447–481.
[5] S. Chakravarthy and S. Osher, *Numerical experiments with the Osher upwind scheme for the Euler equations*, AIAA J., 21 (1983), pp. 1241–1248.
[6] S. Osher, *Riemann solvers, the entropy condition, and difference approximations*, SIAM J. Numer. Anal., 21 (1984), pp. 217–235.
[7] S. Osher and S. Chakravarthy, *High resolution schemes and the entropy condition*, SIAM J. Numer. Anal., 21 (1984), pp. 955–984.
[8] D. Lanser, J. Blom and J. Verwer, *Spatial discretization of the shallow water equations in spherical geometry using Osher's scheme*, J. Comput. Phys., 165 (2000), pp. 542–565.
[9] R. Fedkiw, G. Sapiro and C. Shu, *Shock capturing, level sets, and PDE based methods in computer vision and image processing: a review of Osher's contributions*, J. Comput. Phys., 185 (2003), pp. 309–341.
[10] L. Qiang and W. Zhao, *Computation of turbulence flow on hybrid grids using k-w turbulence model and Osher scheme*, Trans. Nanjing University Aeronaut. Astronaut., 21 (2004), pp. 94–97.
[11] G. Coclite, S. Mishra and N. Risebro, *Convergence of an Engquist-Osher scheme for a multi-dimensional triangular system of conservation laws*, Math. Comput., 79 (2010), pp. 71–94.
[12] J. Qiu, B. Khoo and C. Shu, *A numerical study for the performance of the Runge Kutta discontinuous Galerkin method based on different numerical fluxes*, J. Comput. Phys., 212 (2006), pp. 540–565.
[13] J. Qiu, *Development and comparison of numerical fluxes for LWDG methods*, J. Comput. Phys., 1 (2008), pp. 1–32.
[14] C. Lu, J. Qiu and R. Wang, *A numerical study for the performance of the WENO schemes based on different numerical fluxes for the shallow water equations*, J. Comput. Math., 28 (2010), pp. 807–825.
[15] J. Felcman and O. Havle, *On a numerical flux for the shallow water equations*, Appl. Math. Comput., 217 (2011), pp. 5160–5170.
[16] K. Peery and S. Imlay, *Blunt-body flow simulations*, AIAA, (1988), 2904.

https://doi.org/10.4208/aamm.2014.m469 Published online by Cambridge University Press

[17] M. LIOU AND C. STEFFEN, *A new flux splitting scheme*, J. Comput. Phys., 107 (1993), pp. 23–39.
[18] H. LIN, *Dissipation additions to flux-difference splitting*, J. Comput. Phys., 117 (1995), pp. 20–27.
[19] R. SANDERS, E. MORANO AND M. DRUGUETZ, *Multidimensional dissipation for upwind schemes: stability and applications to gas dynamics*, J. Comput. Phys., 145 (1998), pp. 511–537.
[20] M. PANDOLFI AND D. D'AMBROSIO, *Numerical instabilities in upwind methods: analysis and cures for the "carbuncle" phenomenon*, J. Comput. Phys., 166 (2001), pp. 271–301.
[21] Y. REN, *A robust shock-capturing scheme based on rotated Riemann solvers*, Comput. Fluids, 32 (2003), pp. 1379–1403.
[22] S. SPEKREIJSE, *Multiple grid and Osher's scheme for the efficient solution of the steady Euler equations*, Appl. Numer. Math., 2 (1986), pp. 475–493.
[23] P. JACOBS, *Approximation Riemann solver for hypervelocity flows*, AIAA J., 30 (1992), pp. 2558–2561.
[24] J. AMALADAS AND H. KAMATH, *Accuracy assessment of upwind algorithms for steady-state computations*, Comput. Fluids, 27 (1998), pp. 941–962.
[25] N. FRINK, *Upwind scheme for solving the Euler equations on unstructured tetrahedral meshes*, AIAA J., 30 (1991), pp. 70–77.
[26] B. VAN LEER, *Towards the ultimate conservative difference scheme IV. a new approach to numerical convection*, J. Comput. Phys., 23 (1977), pp. 276–299.
[27] B. VAN LEER, *Towards the ultimate conservative difference scheme V. a second-order sequel to Godunov's method*, J. Comput. Phys., 32 (1979), pp. 101–136.
[28] E. TORO, Riemann Solvers and Numerical Methods for Fluid Dynamics, Springer, 1997.
[29] P. WOODWARD AND P. COLELLA, *The numerical simulation of two-dimensional fluid flow with strong shocks*, J. Comput. Phys., 54 (1984), pp. 115–173.
[30] A. NISHINO, T. ISHIKAWA, K. KITAMURA AND Y. NAKAMURA, *Effect of the clearance between two bodies on TSTO aerodynamic heating*, J. Japan Soc. Aer. Space Sci., 53 (2005), pp. 503–509.
[31] K. KITAMURA, E. SHIMA, Y. NAKAMURA AND P. L. ROE, *Evaluation of Euler fluxes for hypersonic heating computations*, AIAA J., 48 (2010), pp. 763–776.
[32] K. KITAMURA, *A further survey of shock capturing methods on hypersonic heating issues*, AIAA paper, 2013–2698.

https://doi.org/10.4208/aamm.2014.m469 Published online by Cambridge University Press